

Journal of Materials Chemistry A

Materials for energy and sustainability

Accepted Manuscript

This article can be cited before page numbers have been issued, to do this please use: J. Xian, Z. Mi, P. Tonanon, X. Cao, R. D. Webster and W. R. Leow, *J. Mater. Chem. A*, 2026, DOI: 10.1039/D6TA02361D.



This is an Accepted Manuscript, which has been through the Royal Society of Chemistry peer review process and has been accepted for publication.

Accepted Manuscripts are published online shortly after acceptance, before technical editing, formatting and proof reading. Using this free service, authors can make their results available to the community, in citable form, before we publish the edited article. We will replace this Accepted Manuscript with the edited and formatted Advance Article as soon as it is available.

You can find more information about Accepted Manuscripts in the [Information for Authors](#).

Please note that technical editing may introduce minor changes to the text and/or graphics, which may alter content. The journal's standard [Terms & Conditions](#) and the [Ethical guidelines](#) still apply. In no event shall the Royal Society of Chemistry be held responsible for any errors or omissions in this Accepted Manuscript or any consequences arising from the use of any information it contains.

1 **Vacancy-defective spinel NiCo₂O₄ enables high-valent Ni/Co species and**
2 **adsorbate binding for the electrocatalytic upcycling of polybutylene**
3 **succinate plastics**

4 Jiahui Xian^{1,2}, Ziyu Mi^{1,2}, Panyawut Tonanon¹, Xun Cao², Richard D. Webster¹ and Wan Ru
5 Leow^{1,2*}

6 ¹School of Chemistry, Chemical Engineering and Biotechnology, Nanyang Technological
7 University; 21 Nanyang Link, Nanyang Technological University, Singapore 637371,
8 Republic of Singapore

9 ²Institute of Sustainability for Chemicals Energy and Environment (ISCE²), Agency for
10 Science, Technology and Research (A*STAR); 1 Pesek Road Jurong Island, Singapore 627833,
11 Republic of Singapore

12 *Corresponding authors. Email: wanru.leow@ntu.edu.sg



13 **Abstract**

14 Electroreforming polybutylene succinate (PBS) plastics waste and NO_x into value-added
15 chemicals is a promising strategy to mitigate environmental pollution. However, achieving
16 high activity and controllable selectivity remains challenging especially at industrially relevant
17 current densities, due to the complex multi-step dehydrogenation of alcohol intermediates and
18 competing oxygen evolution reaction. Here, we report a vacancy-defective spinel-type
19 NiCo_2O_4 electrocatalyst for the enhanced electrooxidation of 1,4-butanediol, a monomer
20 derived from PBS plastic. Mechanistic studies revealed that the catalyst facilitates the
21 generation of high-valent Ni/Co species and regulates the adsorption of oxygen-containing
22 intermediates, thereby boosting catalytic activity via a OH^* -participated mechanism. By
23 pairing PBS hydrolysate oxidation with NO_x reduction reaction in a membrane electrode
24 assembly, the system achieved a cell voltage of 1.42 V at 400 mA cm^{-2} , while maintaining
25 continuous operation for over 100 hours with combined Faradaic efficiencies exceeding 175%.
26 High-purity SA and NaHCO_3 products can be separated from the post-reaction anolyte via
27 CO_2 -assisted acidification-precipitation. The obtained SA can further react with concentrated
28 NH_3 in the catholyte to yield valuable succinimide. This work provides a practical approach
29 for the efficient upcycling of sustainable plastic and NO_x into valuable products, enabled
30 through tailored catalyst design and system configuration.



31 Introduction

32 Plastics are ubiquitous in modern society due to low cost, wide-spread applications and
33 durability.¹⁻³ However, the disposal of end-of-life plastics poses a significant problem - the
34 environmental accumulation of plastic waste is projected to reach 12,000 million metric tons
35 by 2050.⁴⁻⁷ An example of such plastics is polybutylene succinate (PBS), with global
36 production exceeding 120,000 tons/year due to applications in packaging, agriculture and
37 textiles.^{8,9} While it can be argued that PBS plastics are biodegradable, the degradation process
38 is typically slow and converts a valuable carbon source into CO₂ emissions.^{10,11} From a
39 chemistry perspective, PBS is produced via the polycondensation of 1,4-butanediol (BDO) and
40 succinic acid (SA), which means that end-of-life PBS represents a rich reservoir of valuable C₄
41 platform chemicals. SA is a vital C₄ diacids platform chemical for producing high-demand
42 industrial commodities.^{12,13} SA can also undergo amination to form succinimide, a privileged
43 heterocyclic scaffold that is widely utilized as a versatile intermediate in organic synthesis and
44 pharmaceutical development.¹² Thus, instead of conventional disposal or passive
45 biodegradation, upcycling PBS into high-value chemicals offers a more sustainable strategy
46 that simultaneously achieves plastic waste management and carbon resource recovery.

47 The electrocatalytic reforming of hydrolyzed polyester plastics into value-added chemicals,
48 which can be powered by renewable electricity under mild conditions, has recently emerged as
49 a sustainable and economically attractive route for plastic upcycling.^{1,14-19} This typically
50 involves the oxidation of binary primary alcohols to dicarboxylic acids, for which Ni-based
51 materials have been extensively explored as efficient electrocatalysts, with *in situ* generated



52 high-valent Ni species serving as the key active phase.²⁰⁻²² However, achieving high activity
53 and controllable selectivity remains challenging especially at industrially relevant current
54 densities, due to the complex multi-step dehydrogenation of alcohol intermediates and
55 competing oxygen evolution reaction (OER).²³ Conversely, Co-based catalysts often exhibit
56 oxidation activity at significantly lower onset potentials.²⁴ Thus, integrating Ni and Co sites is
57 expected to generate a synergistic effect that can enhance activity and selectivity toward the
58 oxidation of binary primary alcohols, while suppressing the competing OER through electronic
59 redistribution and optimized adsorption strength.²⁵⁻²⁷ To effectively harness such synergistic
60 interactions, it is highly desirable to construct catalyst structures that can accommodate
61 multiple catalytic sites, regulate their electronic structure and optimize alcohol oxidation while
62 suppressing the competing OER. Spinel-type oxides have recently emerged as promising
63 candidates in this regard, owing to their unique crystal framework that enables the coexistence
64 of multiple metal cations in distinct coordination environments that facilitates efficient charge
65 transfer and redox cycling.²⁸⁻³⁰ These features make spinel oxides particularly attractive for
66 polyol oxidation reactions involving complex multi-step dehydrogenation processes, in order
67 to enable efficient and selective production of dicarboxylic acids.

68 In this work, we report a self-supported NiCo₂O₄ catalyst grown on nickel foam for enhanced
69 electrocatalytic BDO oxidation reaction (BOR). The electrocatalyst achieved high Faradaic
70 efficiencies >87% towards SA across a wide current density range of 200-1000 mA cm⁻².
71 Operando spectroelectrochemical studies and theoretical calculations reveal that the
72 incorporation of Ni into the octahedral Co sites of spinel structures induces the formation of



73 vacancy defects and electronic redistribution. This facilitates the *in situ* generation of
74 CoOOH/NiOOH active species and optimizes the adsorption strength of oxygen-containing
75 intermediates, thereby enhancing BOR catalytic activity via an *OH-mediated oxidation
76 mechanism. We further demonstrated a paired electrocatalytic BOR||NO_xRR system for the
77 simultaneous valorization of PBS hydrolysate and nitrogen oxide (NO_x) (Fig. 1a). Through a
78 membrane electrode assembly (MEA), we achieved industrial-level current density of 400 mA
79 cm⁻² at a low voltage of 1.42 V, as well as 100 hours of stable operation with combined Faradaic
80 efficiencies exceeding 175%. This is integrated with a CO₂-assisted precipitation that enables
81 the recovery of high-purity SA and NaHCO₃ from the post-reaction anolyte. Techno-economic
82 analysis (TEA) confirms the economic viability of this integrated electrocatalytic valorization
83 and product separation system. The obtained SA can be further reacted with concentrated NH₃
84 in the catholyte to yield valuable succinimide.

85 Results

86 A series of M-doped nickel and cobalt oxides (M = Fe, Co, Cu, Zn) were synthesized on nickel
87 foam (NF) substrate (defined as Ni_xM_yO_z) via a hydrothermal method followed by calcination,
88 and their propensity for electrocatalytic BOR was screened in a three-electrode H-type cell.
89 We first performed linear sweep voltammetry (LSV) to evaluate the electrocatalytic activity of
90 catalysts. Compared to other synthesized electrocatalysts, NiCo₂O₄ exhibited a lower BOR
91 potential of 1.41 V vs. RHE to reach the current density of 100 mA cm⁻² (Fig. 1b). Additionally,
92 NiCo₂O₄ showed the lowest Tafel slope of 54.6 mV dec⁻¹ among all catalysts studied (Fig. S1),
93 which suggests significantly faster BOR kinetics. The double-layer capacitance (*C_{dl}*) of



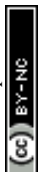
94 NiCo₂O₄ is also significantly higher at 123.8 mF cm⁻², which indicates larger electrochemical
95 active area and more exposed active sites (Fig. 1c and Fig. S2). The electrocatalytic BOR
96 activity of the synthesized electrocatalysts was then evaluated through chronoamperometry at
97 1.50 V vs. RHE, in an electrolyte comprising 1.0 M NaOH and 0.1 M BDO, after which the
98 liquid products were analyzed using ¹H nuclear magnetic resonance (NMR) spectroscopy (Fig.
99 S3). Among all synthesized electrocatalysts, NiCo₂O₄ delivered SA as the main product with
100 the highest activity, as reflected by its Faradaic efficiency of 95.5(±2.8)%, selectivity of
101 89.2(±3.5)% and yield of 87.9(±4.5)% (Fig. 1d and Fig. S4). The electrocatalytic activity of
102 Co₃O₄ and NiO are significantly inferior in comparison, which suggests a synergistic effect
103 from integrating Ni and Co sites in NiCo₂O₄. Overall, the electrocatalytic activity of the
104 synthesized electrocatalysts followed the trend: NiCo₂O₄ > Co₃O₄ > NiZnO > NiCuO >
105 NiFe₂O₄ > NiO.

106 The electrocatalysts were then characterized to understand the difference in electrocatalytic
107 activity. X-ray diffraction (XRD) revealed that the crystalline structures of the electrocatalysts
108 were nickel-based or cobalt-based oxides (Fig. S5-S10). For NiCo₂O₄ and Co₃O₄, the
109 diffraction peaks at 31.1°, 36.7°, 59.1° and 64.9° correspond to the (220), (311), (511) and
110 (440) planes of the cubic spinel structure. Scanning electron microscopy (SEM) revealed the
111 morphology of NiO, NiFe₂O₄, and NiZnO catalysts to be uniform nanosheets on the NF
112 substrate (Fig. S5-S8). In contrast, the introduction of Co metal source during synthesis, such
113 as in NiCo₂O₄ and Co₃O₄, led to a distinct one-dimensional nanostructure. Notably, the
114 NiCo₂O₄ catalyst existed as uniformly distributed nanowire arrays on the NF substrate (Fig. 2a



115 and Fig. S11). Elemental mappings showed that Ni, Co and O were uniformly distributed
116 throughout the whole nanowire (Fig. 2b). High-resolution transmission electron microscopy
117 (HRTEM) images display distinct lattice spacings of 0.248 nm and 0.206 nm, which can be
118 assigned to the (311) and (400) planes of NiCo₂O₄ (Fig. 2c). Abundant vacancy defects were
119 observed by HRTEM and corresponding integrated pixel intensity profile (Fig. 2c and Fig.
120 S12). These defects likely originated from the partial substitution of Co with Ni of similar
121 cation radius, which would provide abundant active sites for the adsorption and activation of
122 oxygen-containing intermediates.²⁹

123 The Raman spectra of NiCo₂O₄ and Co₃O₄ exhibit five typical characteristic peaks in 191.4,
124 477.8, 517.3, 615.1 and 684.8 cm⁻¹, corresponding to the F_{2g}¹, E_g, F_{2g}², F_{2g}³ and A_{1g} vibrational
125 modes of spinel Co₃O₄, respectively (Fig. 2d). The F_{2g}¹ and A_{1g} signals can be attributed to the
126 asymmetric and symmetrical stretching vibration of Co²⁺-O bond in tetrahedral coordination
127 sites and Co³⁺-O bond in octahedral coordination sites, respectively. Compared to Co₃O₄, the
128 NiCo₂O₄ showed an obvious redshift in its A_{1g} Raman signal, while its F_{2g}¹ signal remained
129 unshifted, which suggests that the incorporated Ni mainly occupied the octahedral coordination
130 sites. Meanwhile, the broader and weaker A_{1g} signal in NiCo₂O₄ indicates lattice distortion or
131 deficient coordination due to Ni incorporation into the Co₃O₄ lattice, which promotes the
132 formation of vacancy defects.^{29, 31} The high-resolution Ni 2*p* X-ray photoelectron spectroscopy
133 (XPS) spectra can be deconvoluted into two spin-orbit doublets corresponding to Ni²⁺ (854.3
134 and 871.8 eV) and Ni³⁺ (855.7 and 873.2 eV), along with the accompanying satellite peaks
135 (Fig. 2e and Table S1). Notably, the Ni²⁺ 2*p* peaks in NiCo₂O₄ shifted to higher binding energy



136 compared to that in NiO, which suggests electronic interaction between Ni and the Co. On the
137 other hand, Co 2*p* XPS spectra displayed two characteristic spin-orbital doublets at
138 approximately 779.4 / 794.6 eV and 781.1 / 796.5 eV, which can be attributed to Co³⁺ and Co²⁺
139 respectively. A negative shift of ~0.3 eV was observed for the Co 2*p* peaks in NiCo₂O₄ relative
140 to those in Co₃O₄, and the ratio of Co²⁺/Co³⁺ in NiCo₂O₄ (1.48) is higher than that of Co₃O₄
141 (1.41), which suggests the formation of lower Co valence state (Fig. 2f and Table S2). These
142 results further indicate the introduced Ni atoms preferentially occupy the octahedral Co³⁺ sites
143 within the spinel lattice, which is in agreement with the observed Raman shifts. The O 1s
144 spectra of the electrocatalysts show three peaks at 529.4, 531.1 and 532.9 eV (Fig. S13 and
145 Table S3), corresponding to the lattice oxygen (O_a), chemisorbed oxygen (O_b) and surface
146 oxygen (O_c), respectively. NiCo₂O₄ exhibits higher O_b/O_a ratio, suggesting increased surface
147 oxygen vacancies when the spinel lattice was disrupted through the introduction of Ni atoms.³²
148 The electron paramagnetic resonance (EPR) spectrum of NiCo₂O₄ exhibits a distinct and
149 symmetric Lorentzian-shaped signal, a feature characteristic of electrons trapped in oxygen
150 vacancies, while a much weaker signal was observed for Co₃O₄ (Fig. S14). All above results
151 confirm that introducing Ni into the Co₃O₄ spinel structure endows NiCo₂O₄ with abundant
152 electroactive sites and vacancy defects, which is crucial for boosting the electrocatalytic BOR
153 performance.

154 Having established the nature of the NiCo₂O₄ electrocatalyst, we investigated its
155 electrochemical BOR activity in 1.0 M NaOH containing 0.1 M BDO electrolyte. Upon
156 increasing the applied potential from 1.45 V to 1.50 V vs. RHE, the Faradaic efficiency towards



157 SA significantly increased from 76.1(\pm 1.1)% to 95.5(\pm 2.8)%, and the yield rose from 51.6
158 (\pm 2.5)% to 87.9 (\pm 4.5)%. Beyond 1.50 V vs. RHE, NiCo₂O₄ exhibited superior SA production
159 with up to 96.0% Faradaic efficiency, 95.4% yield and 95.6% selectivity (Fig. 3a and Fig. S15),
160 which is competitive with that of previously reported catalysts (Table S4). This means that SA
161 productivity can remain high across a wide range of current densities (200-1000 mA cm⁻²),
162 with Faradaic efficiencies >87%, yields >90% and selectivities >93% (Fig. 3b and Fig. S16).

163 Cyclic voltammetry (CV) revealed a characteristic anodic peak located from 1.35 to 1.45 V vs.
164 RHE, which can be attributed to the oxidation of Ni²⁺/Ni³⁺ and Co²⁺/Co³⁺ redox couples.³³ The
165 incorporation of Ni promotes the pre-oxidation of Co²⁺, thereby enhancing the BOR activity,
166 as evidenced by the appearance of a distinct Co²⁺ pre-oxidation peak at ~1.28 V vs. RHE and
167 more intense oxidation peak in NiCo₂O₄ compared to Co₃O₄ (Fig. 3c). Upon the addition of
168 0.1 M BDO, these oxidation peaks disappear and the anodic current density increases sharply,
169 which confirms the involvement of active Ni and Co species in electrocatalytic BOR (Fig. S17).

170 The CV curves can also provide insights on the adsorption behavior of *OH on the NiCo₂O₄
171 electrocatalyst.^{20,34} Regardless of BDO addition, NiCo₂O₄ electrocatalyst exhibited a higher
172 peak oxidation current for OH⁻ → *OH compared to Co₃O₄ (Fig. S18), indicating that Ni
173 incorporation enhances the generation and adsorption of *OH species. We performed quasi-in-
174 situ EPR using DMPO (5,5-dimethyl-1-pyrroline N-oxide) as a spin-trapping agent, we
175 observed the characteristic 1:2:2:1 quartet signal for DMPO-*OH adduct in the absence of
176 BDO at 1.5 V vs. RHE for 5 min. This provides direct evidence for the electrochemical
177 conversion of OH⁻ to *OH. Upon the addition of BDO, the DMPO-*OH signal intensity



178 decreased and DMPO- \cdot R signal appeared, indicating the involvement of \cdot OH in the
179 electrocatalytic BOR process (Fig. S19).

180 Operando electrochemical impedance spectroscopy (EIS) was conducted to further investigate
181 high electrocatalytic BOR activity (Fig. S20). The Bode plots exhibited distinct features in the
182 high-frequency region under potentials of 1.05-1.40 V vs. RHE, corresponding to the
183 electrooxidation of $\text{Ni}^{2+}/\text{Co}^{2+}$ to $\text{Ni}^{3+}/\text{Co}^{3+}$. In the presence of BDO, low-frequency signals
184 emerged at potentials above 1.35 V vs. RHE, which suggests that the BOR becomes the
185 dominant electrochemical process. With increasing applied potentials, the lower phase angles
186 indicate more favorable BOR than OER, as well as enhanced interface reactivity. This implies
187 rapid oxidation of absorbed BDO molecules with faster interfacial charge transfer without OER
188 interference. We also observed lower phase angles for NiCo_2O_4 compared to Co_3O_4 , which
189 meant that introducing Ni into the Co_3O_4 cubic spinel structure led to increased BOR activity.

190 We further probed this electrooxidation mechanism by performing a multipotential-step
191 experiment on the NiCo_2O_4 catalyst. The protocol is as follows: (i) 1.5 V vs. RHE to generate
192 high-valent Ni/Co oxidized species, (ii) open circuit potential (OCP), and finally (iii) 1.0 V vs.
193 RHE (Fig. 3d). In the control experiment without BDO, the high-valent Ni/Co oxidized species
194 would revert back to their original valence state at 1.0 V vs. RHE, leading to the observation
195 of a reduction current. With BDO injection at OCP, this reduction current at 1.0 V vs. RHE
196 was smaller, which means that BDO reacted with the electrogenerated high-valent Ni/Co
197 species and caused them to be rapidly consumed. No significant reduction current can be



198 detected if BDO is present from the start, which means that BDO can immediately consume
199 the electrogenerated active species once formed. We then employed *in situ* Raman
200 spectroscopy to gain further insight into the dynamic structural evolution and active sites. For
201 the OER process, NiCo₂O₄ displays five characteristic peaks at OCP, which are associated with
202 the vibrational modes of NiCo₂O₄ spinel structure. As the potential increased to 1.3 V vs. RHE,
203 these peaks gradually diminished. Two new peaks at approximately 457 and 528 cm⁻¹ emerged
204 at 1.4 V vs. RHE and slightly intensified with increased potential, which correspond to the E_g
205 and A_{1g} vibrational modes of Co³⁺-O/Ni³⁺-O bond in CoOOH/NiOOH species (Fig. 3e).^{26, 34}
206 These potential-dependent Raman shifts confirm the *in situ* structural reconstruction of
207 NiCo₂O₄/NF under OER condition, leading to the formation of high-valent Ni/Co
208 (oxy)hydroxide species (CoOOH/NiOOH). In contrast, the NiCo₂O₄ catalyst retained its
209 original spinel structure during BOR. No characteristic peaks for Co³⁺-O/Ni³⁺-O bonds were
210 detected, and the signature peaks of NiCo₂O₄ remained across the entire potential range from
211 OCP to 1.6 V vs. RHE (Fig. 3f). This indicates that BDO molecules react instantly with
212 CoOOH/NiOOH species once generated, such that the consumption rate of these species
213 exceeds the generation rate, which suppresses the competing OER and enables continuously
214 electrogenerated highly active species for efficient BOR. Combined with the insights from
215 cyclic voltammetry, multipotential-step experiment and Raman spectroscopy, this suggests that
216 enhanced generation and adsorption of *OH species is favorable for the BOR mechanism,
217 which can be achieved through the abundant electroactive sites and vacancy defects in NiCo₂O₄.
218 We further tracked the potential-dependent evolution of adsorbed intermediates and products



219 over NiCo₂O₄ catalyst using *in situ* attenuated total reflection surface-enhanced infrared
220 absorption spectroscopy (ATR-SEIRAS). The peak at 1024 cm⁻¹ can be attributed to the C–
221 OH stretching vibration of BDO.^{22, 23} The increase in intensity as the potential shifts from OCP
222 to 1.6 V vs. RHE can be attributed to increased adsorption of BDO on catalyst surface. The
223 peaks at 1225 cm⁻¹ and 1170 cm⁻¹ can be assigned to the C–O stretching vibration of the
224 generated oxygenated molecules. The 1225 cm⁻¹ peak appeared at 1.05 V vs. RHE, while the
225 1170 cm⁻¹ peak emerged at 1.10 V vs. RHE and continuously increased up to 1.60 V vs. RHE.
226 This coincides with the onset potential for the formation of *OH, which further confirms the
227 role of *OH in generating oxygenated molecules during the electrocatalytic BOR process. The
228 peak at 1068 cm⁻¹, which can be attributed to the stretching vibration of the aldehyde group,
229 increased in intensity from 1.25 V vs RHE, which implies that BDO was first oxidized to 4-
230 hydroxybutyric acid.^{35, 36} Two distinct peaks at 1272 and 1624 cm⁻¹, which can be assigned to
231 the C–O and C=O stretching vibration of carboxylate, were also observed at 1.25 V vs. RHE
232 and increased with increasing potential, indicating the generation of SA product (Fig. 3g).³⁵⁻³⁷

233 We corroborated our experimental results with density functional theory (DFT) calculations
234 performed on the optimized stable NiCo₂O₄ and Co₃O₄ model slabs (Fig. S21). As the effective
235 regulation of adsorption behavior is critical for achieving highly selective oxidation, the
236 adsorption of BDO and *OH on the octahedral sites were investigated. For *OH, the octahedral
237 Co sites on NiCo₂O₄ exhibit markedly stronger adsorption (–1.59 eV) than the Co sites on
238 Co₃O₄ (–0.79 eV) and the Ni sites on NiCo₂O₄ (–0.98 eV) (Fig. 4a and Fig. S22). A similar
239 phenomenon is observed for BDO adsorption, with the octahedral Co sites on NiCo₂O₄



240 showing the strongest binding (Fig. 4b and Fig. S23). Projected density of states (PDOS)
241 analysis reveals significant orbital hybridization between Co/Ni 3*d* and O 2*p* states in NiCo₂O₄,
242 suggesting an altered electronic configuration of the adjacent Co atoms upon Ni incorporation.
243 The d-band center (ϵ_d) of the NiCo₂O₄ (-1.43 eV) is closer to the Fermi level than the Co₃O₄
244 (-1.82 eV), indicating stronger antibonding interactions and consequently enhanced adsorption
245 of BDO and *OH species (Fig. 4c). These results collectively demonstrate that Ni incorporation
246 at the octahedral Co sites regulates the electronic structure and enhances the adsorption of
247 oxygen-containing intermediates, thereby promoting the catalytic BOR process. Based on the
248 above evidence, we propose an *OH-participated oxidation pathway (Fig. 4d). Under the
249 electrochemical driving force, BDO molecules and hydroxyl species are initially adsorbed onto
250 the catalyst surface, such that OH⁻ from the electrolyte is converted into surface-bound *OH
251 at the active sites. The generated *OH subsequently attacks the alcoholic hydroxyl groups of
252 the adsorbed BDO molecules, followed by continual oxidative deprotonation to ultimately
253 generate SA product.

254 Finally, we realized overall waste PBS recycling by integrating electrochemical BOR and PBS
255 hydrolysis. The obtained PBS hydrolysate contained only BDO and SA monomers (Fig. S24),
256 which directly served as the anolyte without further purification. The subsequent
257 electrocatalytic upgrading of PBS hydrolysate was coupled with cathodic NO_x reduction, to
258 enable simultaneous valorization of two waste streams into valuable chemicals with improved
259 energy efficiency and process economics at the industrial scale.^{38,39} This paired BOR||NO₂-RR
260 system was assembled using a membrane electrode assembly (MEA) electrolyzer, comprising



261 a NiCo_2O_4 anode and an oxide-derived Cu cathode coated on copper foam (OD-Cu) (Fig. S25).
262 The OD-Cu cathode was fabricated by electrochemically reducing the pre-deposited Cu_xO
263 array (see characterization in Fig. S26). The assembled $\text{BOR}||\text{NO}_2^-$ RR electrolyzer achieved
264 an industrial current density of 400 mA cm^{-2} at a low cell voltage of 1.42 V (Fig. 5a). This cell
265 voltage is significantly lower than that of the $\text{BOR}||\text{HER}$ electrolyzer, which signifies improved
266 reaction kinetics and energy efficiency. The paired-electrosynthesis system demonstrated the
267 robust durability, maintaining Faradaic efficiencies averaging 87.3% and 90.7% towards SA
268 and NH_3 for over 100 hours at an industrial current density of 400 mA cm^{-2} (Fig. 5b). $^1\text{H NMR}$
269 analysis confirms that BDO is predominantly converted to SA (Fig. S27). Ultimately, 27.4 g
270 SA was obtained from 30 g of PBS plastic, with the simultaneous generation of 0.125 M NH_3
271 in the catholyte. Post-reaction characterization of the NiCo_2O_4 anode and OD-Cu/CF cathode
272 showed little change in structure and morphology (Fig. S28 and Fig. S29).

273 We then employed a CO_2 -assisted sequential precipitation method to separate SA from the
274 alkaline electrolyte, which simultaneously yielded NaHCO_3 as a product (Fig. S30).^{22,40}
275 Specifically, excess CO_2 is introduced into the resulting anolyte until the pH reaches 7.8. This
276 neutralized OH^- and led to the precipitation of low-solubility NaHCO_3 , thereby effectively
277 removing Na^+ ions from solution. Hydrochloric acid is added to convert sodium succinate into
278 SA, which can be precipitated by cooling to 2-8°C due to its lower solubility. Overall, this
279 process enabled the recovery of 0.92 g SA (Fig. 5c and Fig. S31) and 5.1 g NaHCO_3 (Fig. S32)
280 from 100 mL of crude anolyte. Techno-economic analysis (TEA) showed that this technology
281 can be economically viable if we assume an electricity cost of $\$0.1 \text{ kWh}^{-1}$ and Faradaic



282 efficiency exceeding 35% (Fig. S33). Our calculations estimate a net revenue of \$602.2 per ton
283 of SA based on electrochemical performance close to that achieved in the MEA (i.e., Faradaic
284 efficiencies of 90% towards SA and NH_3 at current density 400 mA cm^{-2} , cell voltage 1.5 V)
285 (Fig. 5d). The high-purity SA obtained is itself an important platform chemical, but can also
286 react with concentrated NH_3 in the catholyte to generate succinimide (Fig. 5e and Fig. S34),
287 which is a versatile organic synthetic intermediate.

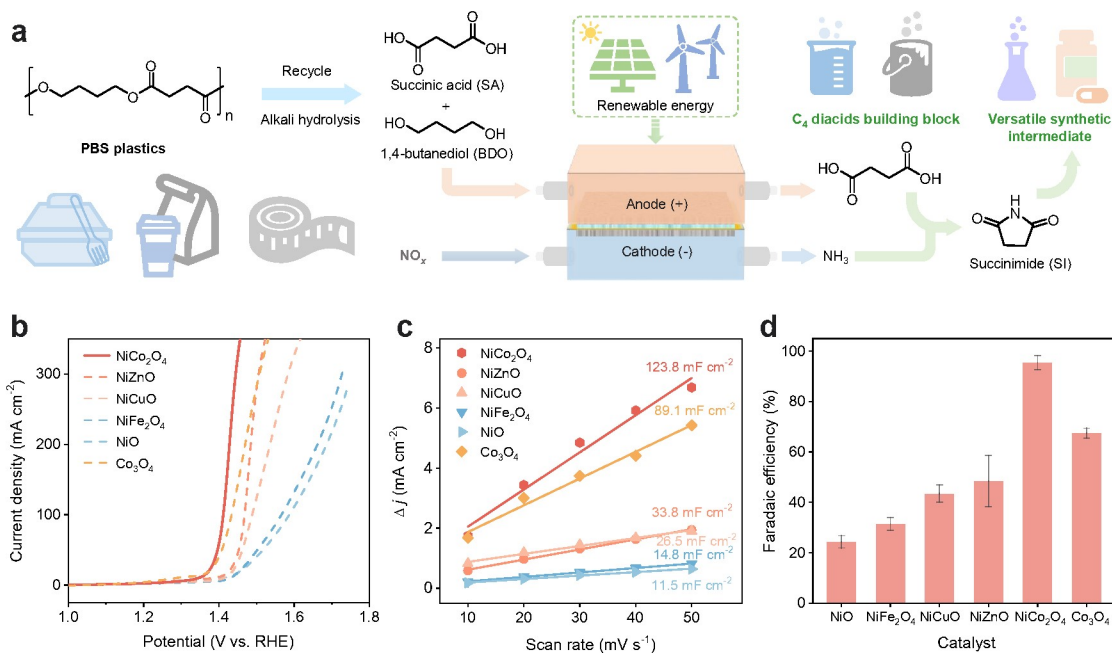
288 Discussion

289 In summary, we report a self-supported NiCo_2O_4 electrocatalyst featuring vacancy defect sites
290 and electronic structure rearrangement, for the electrocatalytic valorization of PBS-derived
291 BDO. The catalyst achieved an industrial-level current density of 1 A cm^{-2} , along with a high
292 Faradaic efficiency ($>87\%$) and yield ($>90\%$) of SA. Both experimental and DFT studies
293 revealed that incorporating Ni into Co octahedral sites modulated the electronic structure and
294 d-band center, which strengthened the adsorption of oxygen-containing intermediates and
295 facilitated pre-oxidation into $\text{CoOOH}/\text{NiOOH}$ active species, thereby boosting BOR activity
296 via an $^*\text{OH}$ -participated oxidation mechanism. We assembled a paired $\text{BOR}||\text{NO}_2^-$ RR system
297 in an MEA configuration, which required only 1.42 V to reach an industrial-level current
298 density of 400 mA cm^{-2} . The stability of the paired $\text{BOR}||\text{NO}_2^-$ RR system was demonstrated
299 through continuous electro-upgrading of PBS-plastic hydrolysate and NO_x waste at Faradaic
300 efficiencies averaging 87.3% and 90.7% for over 100 hours. High-purity SA and NaHCO_3
301 products can be efficiently obtained from the post-reaction anolyte via the CO_2 -assisted
302 sequential precipitation method. The obtained SA can be further converted to succinimide



303 through reaction with concentrated NH_3 in the catholyte. This work presents a practical
304 approach for the electrocatalytic conversion of PBS plastic and NO_x waste into valuable
305 products through tailored catalyst design and system configuration.





306

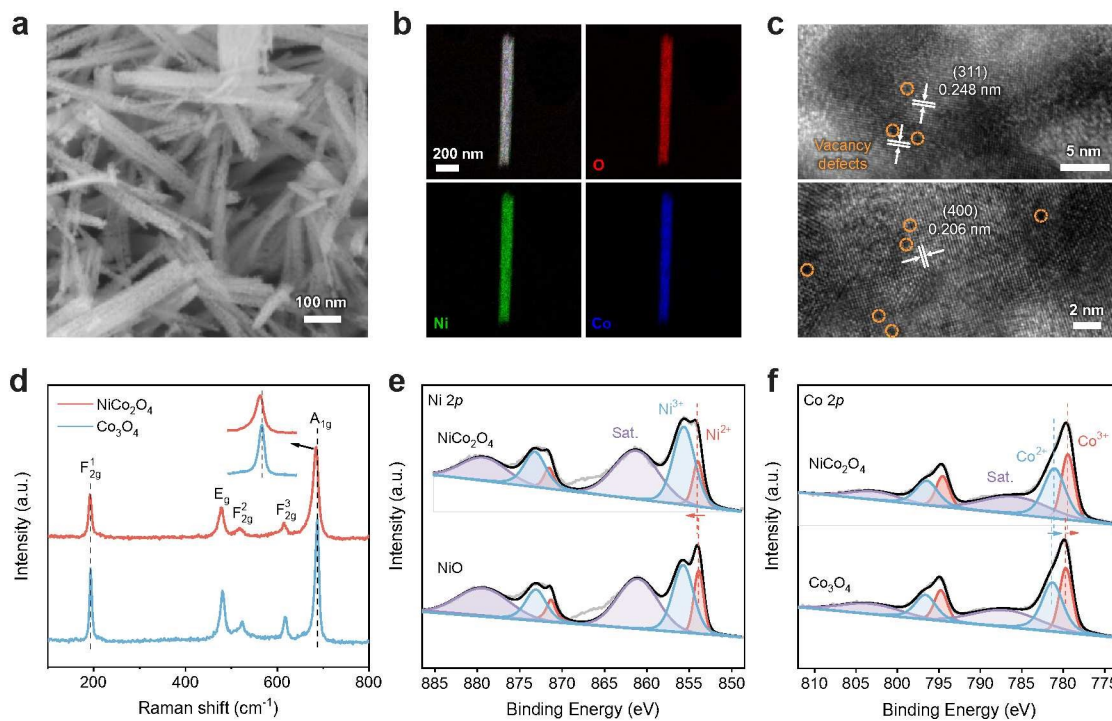
307 **Fig. 1** (a) Schematic illustration of the paired BOR||NO_xRR system for electrocatalytic

308 upgrading of waste pollutants. (b) LSV curves and (c) double layer capacitances of different

309 catalysts for electrocatalytic BOR. (d) Faradaic efficiencies of SA over different

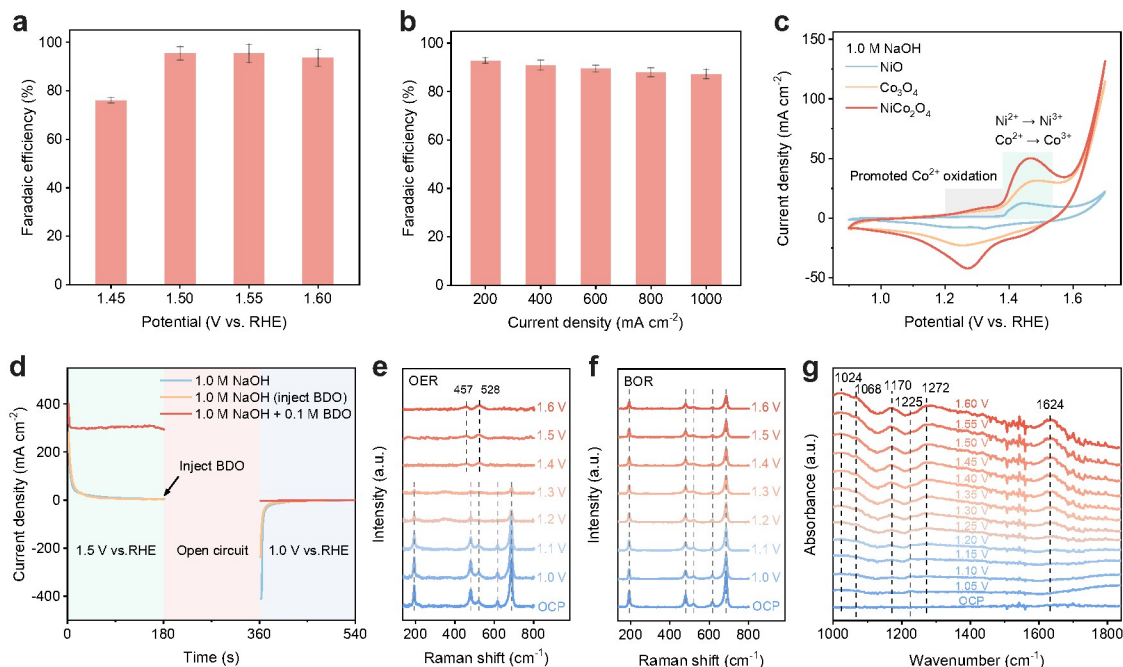
310 electrocatalysts at 1.5 V vs. RHE.





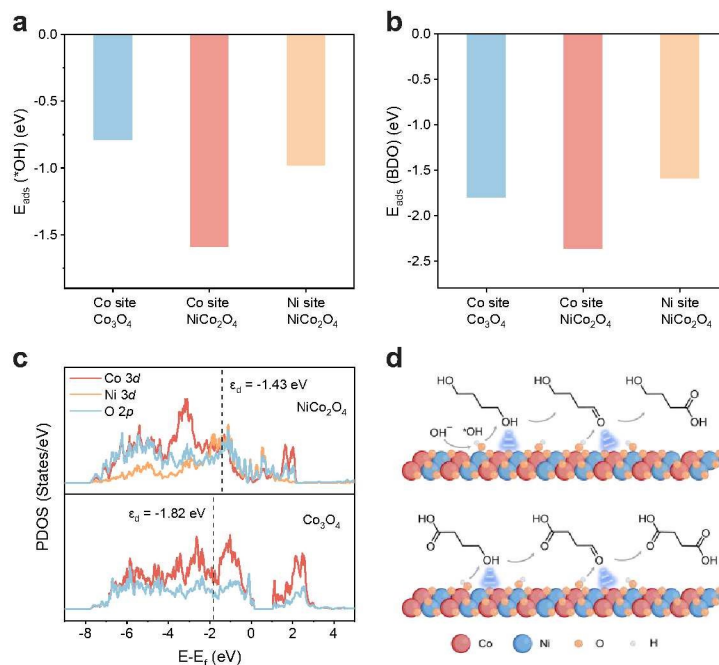
311

312 **Fig. 2** (a) SEM, (b) TEM-EDS elemental mapping and (c) HRTEM images of NiCo₂O₄313 electrocatalyst. (d) Raman spectra of NiCo₂O₄ and Co₃O₄. High-resolution XPS (e) Ni 2*p* and314 (f) Co 2*p* of NiCo₂O₄ and Co₃O₄.



315

316 **Fig. 3** Faradaic efficiency of SA over NiCo₂O₄ at different (a) potentials and (b) current317 densities. (c) CV curves of NiCo₂O₄, Co₃O₄ and NiO in 1 M NaOH solution. (d) Multipotential-318 step curves of NiCo₂O₄ in 1 M NaOH solution with and without 0.1 M BDO injection. In situ319 Raman spectroscopy of NiCo₂O₄ for (e) OER and (f) BOR at varied potentials. (g) In situ FTIR320 spectra of NiCo₂O₄ during the BOR at various potentials.

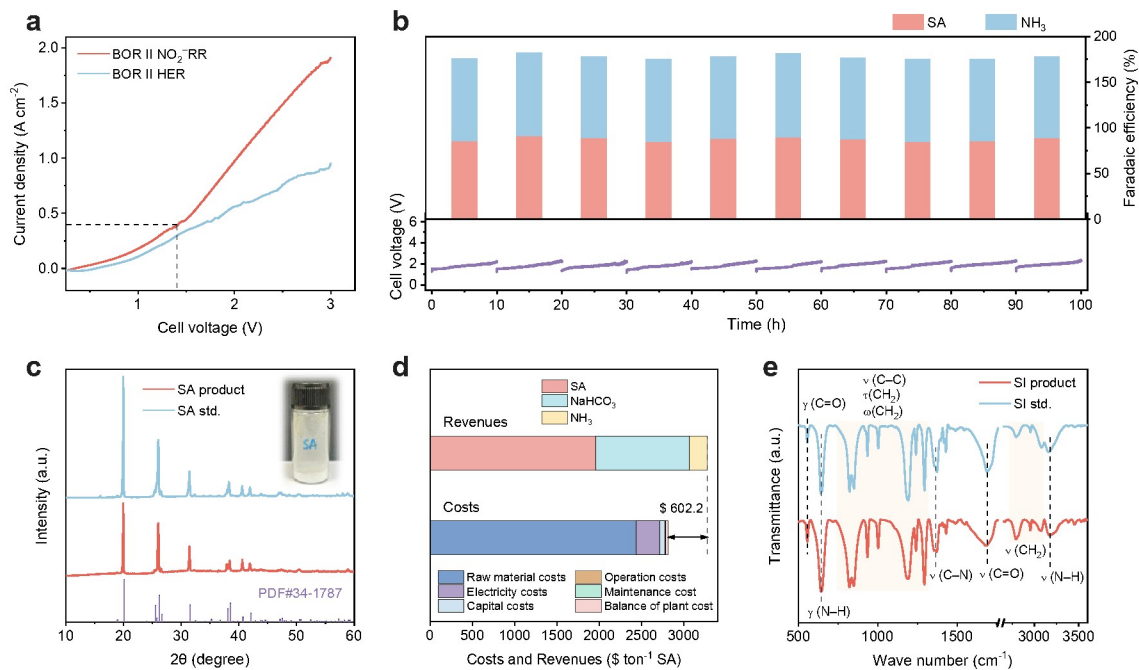


321

322 **Fig. 4** The calculated adsorption energies of (a) $^*\text{OH}$ and (b) BDO on NiCo_2O_4 and Co_3O_4 . (c)323 PDOS profiles of NiCo_2O_4 and Co_3O_4 . (d) Schematic illustration of the proposed BOR324 pathways on the NiCo_2O_4 electrocatalyst.

325





326

327 **Fig. 5** (a) LSV curves of the paired BOR||NO₂-RR and BOR||HER systems. (b)328 Electrochemical upgrading of PBS hydrolysate and NO_x in the MEA electrolyzer at 400 mA329 cm⁻² for 100 hours. (c) XRD patterns of obtained SA product and standard (Inset: photograph330 of the product). (d) TEA of BOR||NO₂-RR electro-upgrading system from PBS plastics. (e)

331 FT-IR spectra of obtained SI product and standard.



332 **References**

- 333 1. K. Zheng, Y. Wu, Z. Hu, S. Wang, X. Jiao, J. Zhu, Y. Sun and Y. Xie, *Chem. Soc. Rev.*,
334 2023, **52**, 8-29.
- 335 2. *Nat. Sustain.*, 2023, **6**, 1137.
- 336 3. J. Chen, L. Zhang, L. Wang, M. Kuang, S. Wang and J. Yang, *Matter*, 2023, **6**, 3322-3347.
- 337 4. R. Geyer, J. R. Jambeck, K. L. Law, *Sci. Adv.*, 2017, **3**, e1700782.
- 338 5. L. D. Ellis, N. A. Rorrer, K. P. Sullivan, M. Otto, J. E. McGeehan, Y. Román-Leshkov,
339 N. Wierckx and G. T. Beckham, *Nat. Catal.*, 2021, **4**, 539-556.
- 340 6. M.-Q. Zhang, M. Wang, B. Sun, C. Hu, D. Xiao and D. Ma, *Chem*, 2022, **8**, 2912-2923.
- 341 7. D. M. Mitrano and M. Wagner, *Nat. Rev. Mater.*, 2021, **7**, 71-73.
- 342 8. D. Nath, M. Misra, F. Al-Daoud and A. K. Mohanty, *RSC Sustainability*, 2025, **3**, 1267-
343 1302.
- 344 9. INDUSTRY RESEARCH, [https://www.industryresearch.biz/market-](https://www.industryresearch.biz/market-reports/polybutylene-succinate-market-114054)
345 [reports/polybutylene-succinate-market-114054](https://www.industryresearch.biz/market-reports/polybutylene-succinate-market-114054), (accessed March 2026).
- 346 10. T.-Y. Liu, D. Huang, P.-Y. Xu, B. Lu, G.-X. Wang, Z.-C. Zhen and J. Ji, *ACS Sustainable*
347 *Chem. Eng.*, 2022, **10**, 3191-3202.
- 348 11. Y. Zhu, X. Che, F. Yuan, R. Jia, P. Chen, L. Shi and L. Huang, *Ind. Eng. Chem. Res.*,
349 2025, **64**, 4627-4636.
- 350 12. V. Kumar, P. Kumar, S. K. Maity, D. Agrawal, V. Narisetty, S. Jacob, G. Kumar, S. K.
351 Bhatia, D. Kumar and V. Vivekanand, *Biotechnol Biofuels*, 2024, **17**, 72.
- 352 13. W. Dessie, X. Luo, G. J. Duns, M. Wang and Z. Qin, *Environ. Technol. Inno.*, 2023, **32**,



- 353 103243.
- 354 14. Q. Hu, Z. Zhang, D. He, J. Wu, J. Ding, Q. Chen, X. Jiao and Y. Xie, *J. Am. Chem. Soc.*,
- 355 2024, **146**, 16950-16962.
- 356 15. S. Zhang, M. Li, Z. Zuo and Z. Niu, *Green Chem.*, 2023, **25**, 6949-6970.
- 357 16. D. Sajwan, A. Sharma, M. Sharma and V. Krishnan, *ACS Catal.*, 2024, **14**, 4865-4926.
- 358 17. Y. X. Leiu, K. M. Lim, Z. J. Chiah, E. S. Z. Mah and W. J. Ong, *EcoEnergy*, 2024, **3**, 217-
- 359 253.
- 360 18. S. Yue, P. Wang, B. Yu, T. Zhang, Z. Zhao, Y. Li and S. Zhan, *Adv. Energy Mater.*, 2023,
- 361 **13**, 2302008.
- 362 19. H. Wu, H. Tian, L. Chen, W. Luo, S. Li, L. Wang, X. Cui and J. Shi, *Adv. Mater.*, 2026,
- 363 **38**, e15766.
- 364 20. Q. Qian, X. He, Z. Li, Y. Chen, Y. Feng, M. Cheng, H. Zhang, W. Wang, C. Xiao, G.
- 365 Zhang and Y. Xie, *Adv. Mater.*, 2023, **35**, e2300935.
- 366 21. M. Song, Y. Wu, Z. Zhao, M. Zheng, C. Wang and J. Lu, *Adv. Mater.*, 2024, **36**, e2403234.
- 367 22. B. Zhou, K. Shi, X. Teng, Z. Li, L. Chen and J. Shi, *Angew. Chem. Int. Ed.*, 2024, **63**,
- 368 e202411502.
- 369 23. J. Yan, Y. Ren, B. Huang, Z. Li, C. Zhao, L. Chen and J. Shi, *J. Am. Chem. Soc.*, 2025,
- 370 **147**, 29340-29348.
- 371 24. Y. Lu, T. Liu, C. L. Dong, C. Yang, L. Zhou, Y. C. Huang, Y. Li, B. Zhou, Y. Zou and S.
- 372 Wang, *Adv. Mater.*, 2022, **34**, e2107185.
- 373 25. D. Chen, Y. Ding, X. Cao and L. Sun, *Appl. Catal. B: Environ. Energy*, 2025, **378**, 125539.



- 374 26. J. Woo, J. Choi, J. Choi, M. Y. Lee, E. Kim, S. Yun, S. Yoo, E. Lee, U. Lee, D. H. Won,
375 J. H. Park, Y. J. Hwang, J. S. Yoo and D. K. Lee, *Adv. Funct. Mater.*, 2025, **35**, 2413951.
- 376 27. W. Wang, X. He, Z. Tu, D. Xiong, S. Dong, T. Zhang, D. Wu, J. Wang and Z. Chen, *ACS*
377 *Catal.*, 2025, **15**, 9574-9583.
- 378 28. B. He, F. Bai, P. Jain and T. Li, *Small*, 2025, **21**, e2411479.
- 379 29. W. Luo, H. Tian, Q. Li, G. Meng, Z. Chang, C. Chen, R. Shen, X. Yu, L. Zhu, F. Kong,
380 X. Cui and J. Shi, *Adv. Funct. Mater.*, 2024, **34**, 2306995.
- 381 30. M. Wang, X. Feng, S. Li, Y. Ma, Y. Peng, S. Yang, Y. Liu, H. Lei, J. Dang, W. Zhang, R.
382 Cao and H. Zheng, *Adv. Funct. Mater.*, 2024, **34**, 2410439.
- 383 31. Z. Chen, G. Zhang, H. Yang, Y. Zhao, A. Pei, P. Wang, J. Yang, J. Zhang, P. Sun, H. Qin,
384 J. Zhan, J. Peng, W. H. Huang, L. Zhou and G. Chen, *ACS Nano*, 2025, **19**, 26572-26582.
- 385 32. R. An, C. Wang, Y. Li, Y. Di, F. Li, F. Li, L. Sun and X. Wu, *ACS Nano*, 2025, **19**, 17490-
386 17502.
- 387 33. M. Jiang, Y. Yang, Y. Wang, Y. Wang, M. Ratova and D. Wu, *Green Chem.*, 2025, **27**,
388 9978-9991.
- 389 34. X. Jiang, X. Ma, Y. Yang, Y. Liu, Y. Liu, L. Zhao, P. Wang, Y. Zhang, Y. Lin and Y.
390 Wei, *Nanomicro Lett.*, 2024, **16**, 275.
- 391 35. F. Kang, Q. Wang, D. Du, L. Wu, D. W. F. Cheung and J. Luo, *Angew. Chem. Int. Ed.*,
392 2025, **64**, e202417648.
- 393 36. D. Du, P. Liu, Z. Teng, T. Chen, J. Zhu, B. Shao and J. Luo, *ACS Catal.*, 2025, **15**, 3038-
394 3045.



- 395 37. X. Jiang, K. Zhao, H. Feng, L. Ke, X. Wang, Y. Liu, L. Li, P. Sun, Z. Chen, Y. Sun, Z.
396 Wang, L. Yu and N. Yan, *J. Am. Chem. Soc.*, 2025, **147**, 13471-13482.
- 397 38. L. Xia, K. Zhao, S. Kadam, M. D. Blanco-González, M. D. Hernández Alonso and F. P.
398 García de Arquer, *Joule*, 2025, **9**, 102049.
- 399 39. J. Qi, Y. Xia, X. Meng, J. Li, S. Yang, H. Zou, Y. Ma, Y. Zhang, Y. Du, L. Zhang, Z. Lin
400 and J. Qiu, *Adv. Mater.*, 2025, **37**, e2419058.
- 401 40. D. Xiong, X. He, Z. Zhu, T. Liu, D. Wu, Y. Zou and Z. Chen, *Adv. Funct. Mater.*, 2026,
402 **36**, e18434.

403 **Acknowledgements**

404 This work is supported by the National Research Foundation Fellowship (NRFF16-2024-0034).

405 **Author contributions**

406 W.R.L. and J.X. conceived the idea, designed the experiments, and co-wrote the manuscript.

407 W.R.L. supervised the project. J.X. carried out the material synthesis and characterization,

408 electrochemical measurements, and analyzed the data. Z.M. performed SEM measurement. P.T.

409 and R.D.W. performed the EPR measurement. X.C. performed TEM characterization. All

410 authors discussed the results and assisted during manuscript preparation.

411 **Competing interests**

412 The authors declare no competing interests.



The data supporting this article have been included as part of the supplementary information (SI). Supplementary information is available.

[View Article Online](#)

DOI: 10.1039/D6TA02361D

